Scripta Materialia 209 (2022) 114379

Contents lists available at ScienceDirect

Scripta Materialia

journal homepage: www.elsevier.com/locate/scriptamat

Viewpoint set

Shock-induced amorphization in medium entropy alloy CoCrNi

Wu-Rong Jian[a,*], Zhuocheng Xie[b,c], Shuozhi Xu[a], Xiaohu Yao[b,c], Irene J. Beyerlein[a,d,1]

[a] Department of Mechanical Engineering, University of California, Santa Barbara, CA 93106-5070, USA
[b] State Key Laboratory of Subtropical Building Science, South China University of Technology, Guangzhou, Guangdong 510640, P. R. China
[c] Department of Engineering Mechanics, South China University of Technology, Guangzhou, Guangdong 510640, P. R. China
[d] Materials Department, University of California, Santa Barbara, CA 93106-5050, USA

ARTICLE INFO

Article history:
Received 16 August 2021
Revised 4 October 2021
Accepted 27 October 2021

Keywords:
Impact behavior
High-speed deformation
Amorphization
Microstructure
Molecular dynamics

ABSTRACT

We perform molecular dynamics simulations to investigate shock-induced amorphization in CoCrNi, a medium entropy alloy (MEA) and its mean-field variant without lattice distortion. We show that a critical velocity exists above which amorphization occurs. At a low shock velocity of 800 m/s, dislocation slip and twins dominate and amorphization does not happen, but as the shock velocity increases, the deformation mechanism transitions from slip and twinning to solid-state amorphization. Under ultra-high shock velocities, extensive amorphization occurs, following the precursor of shock wave, eliminating anisotropy in spall strength. Compared to the mean-field model, lattice distortion in the MEA causes substantially more amorphization, resulting in a lower spall strength, since voids nucleate and grow preferentially in the amorphous regions.

In the past decade, multi-principal element alloys (MPEAs), including medium entropy alloys (MEAs) and high entropy alloys, have been the focus of intense study [1,2], due to their extraordinary mechanical performance compared to traditional metallic alloys [3,4]. MPEAs are crystalline metals that contain three or more elements in nearly equal portions. To compare their performance against widely used metals and alloys, they are tested under quasi-static rates lower than 10^{-1} s^{-1}. Through this, MPEAs have demonstrated high strength [5,6], fracture toughness [7,8], and creep resistance [9]. When the strain rate is increased to medium rates of 10^3–10^5 s^{-1} by Split Hopkinson Bars [10–14], MPEAs retain a higher shear yield strength and better shear toughness than Cu, Ti, and some steels [14,15]. The higher rates associated with shock loading, 10^6–10^{10} s^{-1}, can be achieved by laser-driven or by gas gun tests and a few such shock-loading experiments have been conducted on MPEAs [16–18]. Compared to conventional alloys with shared elements, the MPEAs CoCrFeMnNi and AlCoCrFeNi, exhibit much higher Hugoniot elastic limits (HELs) and phase transition stresses due to their lattice distortion (LD) [16]. Altogether, these results suggest that MPEAs can potentially outperform regular alloys in extreme environments.

During shock compression, solid-state amorphization is a common phenomenon in non-metallic materials, such as olivine [19], boron carbide [20,21], and cristobalite [22]. In general, due to their low glass-forming ability, shock-induced amorphization in metals and metalloids is not as easy as in non-metals [23]. Amorphization in pure metals and metalloids has been observed in extreme conditions, such as in Ta metallic glass produced by high liquid-quenching rates of 10^{14} K/s [24], in localized regions in nanocrystalline Ni manufactured by severe deformation [25], and in Ge under ultrahigh static pressures and elevated temperatures [26] or shock compression [27]. Compared with pure metals, it is easier to activate amorphization in alloys, which have higher glass-forming ability [24,26]. In MPEAs, deformation-mediated amorphization has been observed experimentally under quasi-static and dynamic strain rates below 10^5 s^{-1} [14,28]. Though shock loading experiments have been conducted on MPEAs, whether amorphization occurred or not was not reported [16–18]. However, it is reasonable to speculate the shock-induced amorphization occurs in MPEA, since high strain rate and the associated high shock pressure are prone to trigger the amorphization [29,30].

In this work, we utilize molecular dynamics (MD) simulations to examine the threshold and origin for the shock-induced amorphization in the CoCrNi MEA. MD simulation is an appropriate tool for capturing the structural evolution under ultra-fast loading. Some prior studies have employed MD to analyze shock-induced melting in metallic glasses [31] or nanoporous Cu [32,33], shock damage in graphene [34] and MPEAs [35,36] and shock-induced amorphization in silicon [37]. As shock velocity increases, dislo-

* Corresponding author.
E-mail addresses: wurong@ucsb.edu (W.-R. Jian), yaoxh@scut.edu.cn (X. Yao).

[1] Irene J. Beyerlein was an Editor of the journal during the review period of the article. To avoid a conflict of interest, Irene J. Beyerlein was blinded to the record and another editor processed this manuscript.'

https://doi.org/10.1016/j.scriptamat.2021.114379
1359-6462/

cation slip and twinning are replaced gradually by shock-induced amorphization. At high shock velocities, the significant amorphization leads to loss of crystallographic anisotropy. Compared to its mean-field representation, amorphization is easier to initiate in the CoCrNi MEA under shock loading, due to its LD.

MD simulations are carried out using LAMMPS [38]. We utilize the embedded-atom method (EAM) interatomic potential developed by Li et al [39] to describe the interatomic interactions within the Co-Cr-Ni system. For the mean-field approximation of the interatomic interactions, an average-atom (*A*-atom) EAM potential was developed [40] and can be downloaded from https://github.com/wrj2018/Acta_2020. More details about these two potentials are shown in the supplement.

Two types of atomic models of the CoCrNi crystals are built — one is for the alloy and the other for the *A*-atom material. A single crystalline *A*-atom pure metal model is first built with about 1 million atoms and dimensions $\sim$ 100 nm $\times$ 10.5 nm $\times$ 10.5 nm. The *A*-atom sample is face-centered cubic (FCC) and contains no LD. Next, we randomly replace atoms with Co or Cr or Ni atoms to obtain CoCrNi MEA with an equiatomic composition. To study the crystallographic anisotropy in shock response, we orient the crystal with its *x*-, *y*- and *z*-axes aligned respectively either with the $[1\bar{1}0]$, $[11\bar{2}]$, and [111] directions so that $[1\bar{1}0]$ is the shock direction, or with the [111], $[1\bar{1}0]$, and $[11\bar{2}]$ directions so that [111] is the shock direction. Fig. 1(a) shows the resulting atomic configuration of the CoCrNi MEA crystal. Energy minimization is first performed in all samples, followed by thermostat equilibrium at 300 K for 100 ps under isothermal-isobaric (NPT) ensemble.

Shock loading is applied to all samples, using the microcanonical (NVE) ensemble. To generate a shock wave in the sample, a virtual wall is built on the left surface and made to move at a constant velocity U_p along the positive *x* direction to the right surface. After the compression wave reaches the opposite surface, it is reflected and becomes a release wave. After 11 ps, the virtual wall is removed from the surface, from which another release wave is subsequently generated. When these two release waves come across each other, a tensile region is generated. Once the tensile stress exceeds the strength of the sample, spallation occurs. In this way, the shock process is divided into the compression, release, and tension stages. During shock loading, we apply one-dimension spatial binning analysis with a bin size of 10 Å along the *x* axis to obtain the physical quantities including stress and particle velocity. The crystal analysis method [41] is utilized to characterize stacking faults (SFs), twin boundaries (TBs), and amorphous atoms. Note that the amorphous region represents the region where the atoms do not belong to any crystal arrangement.

Fig. 1 (b–e) shows the shock response at U_p = 1200 m/s in the CoCrNi MEA. For both the $[1\bar{1}0]$ and [111] loading directions, U_p gives rise to a typical elastic-plastic two-wave structure. Fig. 1(b) presents their shock pressure σ_{xx} profiles at 11 ps, when an elastic-plastic two-wave structure is generated. Here, the defects we focus on include the dislocation, twinning and amorphous structure. Fig. 1(d) indicates that no dislocation or twinning initiates in the elastic region, while these two defects are generated in the plastic region. Some discrete amorphous atoms appear in the elastic region due to the lattice disturbance when the elastic wave sweeps. In $[1\bar{1}0]$-loading, the elastic and plastic plateaus for σ_{xx} are compressive, being −48.65 GPa and −70.82 GPa, respectively. In [111]-loading, the elastic response is higher than that in the $[1\bar{1}0]$-loading, up to −63.46 GPa. The plateau in the plastic region, however, is −71.63 GPa, close to that for the $[1\bar{1}0]$-loading. The corresponding shear stress τ in the elastic region is −13.25 GPa for the $[1\bar{1}0]$-loading and −14 GPa for the [111]-loading. In the plastic region, where τ has been partially relieved by the glide of dislocations and formation of twins (Fig. 1(d,e)), τ reduces to −2.24 GPa and −1.89 GPa for the $[1\bar{1}0]$ and [111] loading directions, respectively. Overall, at U_p = 1200 m/s, the CoCrNi MEA is notably elastically, but not plastically, anisotropic in shock compression.

Fig. 2 displays the atomic structures of the CoCrNi MEA in the compression, release, and tension stages for U_p = 800 m/s, 1200 m/s, and 1400 m/s along $[1\bar{1}0]$ and [111] orientations. At U_p = 800 m/s in Fig. 2(a) and (d), dislocations, dissociated SFs, and twins develop in the plastic region of the shock compression stage for both shock directions. More dissociated SFs form than twins (see Figure S1). Compared to the [111]-loading, the $[1\bar{1}0]$-loading prompts more dislocations and SFs, indicating more severe plastic deformation and lower HEL. In addition, more twins are seen in the $[1\bar{1}0]$-loading than in the [111]-loading (see Figure S1). Larger Schmid factors in $[1\bar{1}0]$ loading promotes twinning by offering higher resolved shear stresses than the [111] loading under the same normal shock pressure (see Table S1 in the supplement). After the release wave propagates into the sample at 17 ps, the shock pressure in the compressed region is released, and along with the drop in stress, the mobile dislocation density reduces. After the release wave meets the reflected release wave at 32 ps, a tensile region is generated in the middle of the sample. There, the tensile stress exceeds the sample strength, leading to spallation.

For comparison, Fig. 2(b) and (e) show the deformation processes at U_p = 1200 m/s. They are similar to those at U_p = 800 m/s except that the densities of dislocations and SFs are higher, and more importantly, amorphous regions form behind the shock wave. These amorphous clusters are scattered and small relative to the regions spanned by the dislocations and SFs.

As the shock velocity increases further to 1400 m/s in Fig. 2(c) and (f), the densities of dislocations and SFs in the plastic region in the compression stage do not increase as expected but instead reduce. The reason is due to the occurrence of amorphization in the plastic region. These amorphous areas grow during the release stage and continue growing in the tension stage.

Evidently, a threshold exists for amorphization; the dominant deformation mode in the MEA transitions from dislocation slip and twinning to amorphization as the shock velocity rises from 800 m/s to 1400 m/s. This phenomenon also occurs in the *A*-atom sample (see Figure S2), which has similar average lattice parameter and elastic moduli but lacks the local fluctuations in chemical composition and LD. While amorphization is not special to MEAs, it progresses more easily in the MEA.

Solid-state amorphization is common during the shock compression of many mineral and semiconductors [29]. However, whether amorphization in CoCrNi MEA and *A*-atom sample are solid-state or liquid-state is unclear. To address this, we compare the deformation temperature at different stages of shock loading with the melting point at the corresponding pressure. Since melting point is positively correlated to pressure, shock melting can occur in the compression or release stages. In the compression stage, the ultra-high shock velocity inputs a large amount of energy into the sample, inducing a steep temperature rise, and possibly causing the deformation temperature to exceed the melting point. In the release stage when the shock pressure reduces to nearly zero immediately behind the release wave. Accordingly, the melting point in the released region drops immediately and significantly, while the deformation temperature decreases much more slowly. Therefore, the deformation temperature may lie above the melting point at the released pressure.

Using solid-liquid coexistence (two-phase) simulations [42,43], we calculate the melting point of CoCrNi MEA as a function of pressure in Fig. 3(a). In addition, the temperatures at the shock compression (11 ps) and release (17 ps) stages for U_p = 1400 m/s along $[1\bar{1}0]$ and [111] orientations are extracted from the regions M, M′, N, and N′ in Fig. 2(c) and (f), respectively. Note that regions M, M′, N, and N′ are cut out from the positions near the left edge and have the same cross section as the sample and the width of

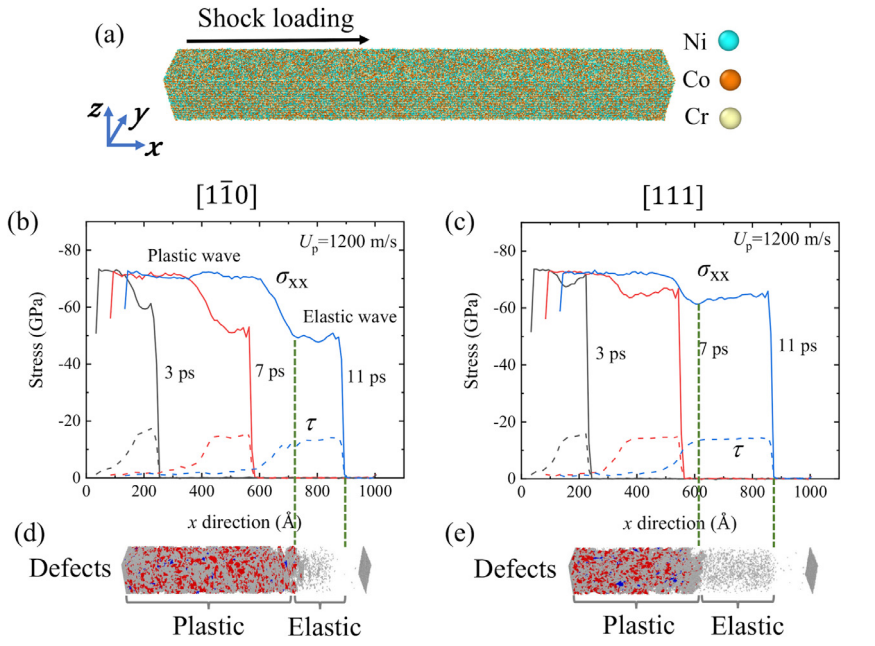

Fig. 1. (a) Atomic configuration of the CoCrNi MEA, in which the Co, Cr, and Ni atoms are randomly distributed. The evolution of the shock pressure σ_{xx} and shear stress τ under shock compression of U_p = 1200 m/s in the (b) [1$\bar{1}$0] and (c) [111] crystallographic directions. The solid lines correspond to σ_{xx}, while the dashed lines are τ. Snapshots of the dislocation, twinning and amorphous structure at 11 ps in the (d) [1$\bar{1}$0] and (e) [111] orientations. Atoms associated with stacking fault (SF), twin boundary (TB), and amorphous structure are colored in red, blue, and gray, respectively. FCC atoms are removed to better visualize the defects. (For interpretation of the references to colour in this figure legend, the reader is referred to the web version of this article.)

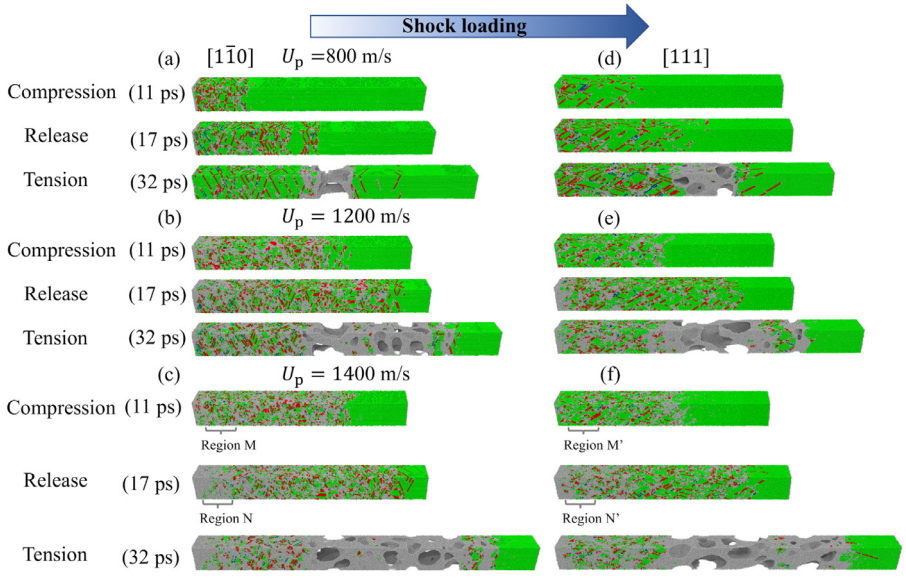

Fig. 2. Snapshots of the atomic structures of the CoCrNi MEA under shock loading of U_p = 800 m/s, 1200 m/s, and 1400 m/s in the (a–c) [1$\bar{1}$0] and (d–f) [111] orientations, respectively. FCC, SF, TB, and amorphous atoms are colored in green, red, blue, and gray, respectively. The arrow indicates the shock direction. For the compression snapshots at 11 ps, the shock wave front has not arrived at the right edge. (For interpretation of the references to colour in this figure legend, the reader is referred to the web version of this article.)

9 nm along the *x* direction. These four temperature points are also added to Fig. 3(a). All of them lie below the melting line, indicating that melting does not occur during both shock compression and release stages, even at U_p = 1400 m/s. By the same analysis, this same conclusion is reached for the *A*-atom material (see Figure S3(a)).

To further confirm whether the shock-induced amorphization is solid-state, we calculate the diffusion coefficient *D* (see supplementary material for details). We estimate *D* from the calculated mean squared displacement (MSD) during an extended equilibrium period of 100 ps in regions M, M′, N, and N′. Fig. 3(b) shows the MSD-time curves, all exhibiting two stages: first, a decrease in slope during 0–40 ps, followed by a nearly constant slope after 40 ps. *D* is the 1/6th of the slope at the latter stage, i.e., $\Delta MSD/6\Delta t$. For regions M, M′, N, and N′, *D* are $3.1\times 10^{-12}m^2/s$, $9.8\times 10^{-13}m^2/s$, $4.0\times 10^{-11}m^2/s$, and $5.3\times 10^{-12}m^2/s$, respectively. These values are all two to four orders of magnitude smaller than $10^{-9}m^2/s$, the typical value for liquid [32,44]. Thus, regions M, M′, N, and N′ are still solid and amorphization within them is solid-state. In Figure S3(b), the calculation is repeated for the *A*-atom metal at U_p = 1400 m/s, confirming that solid-state amorphization occurs as well.

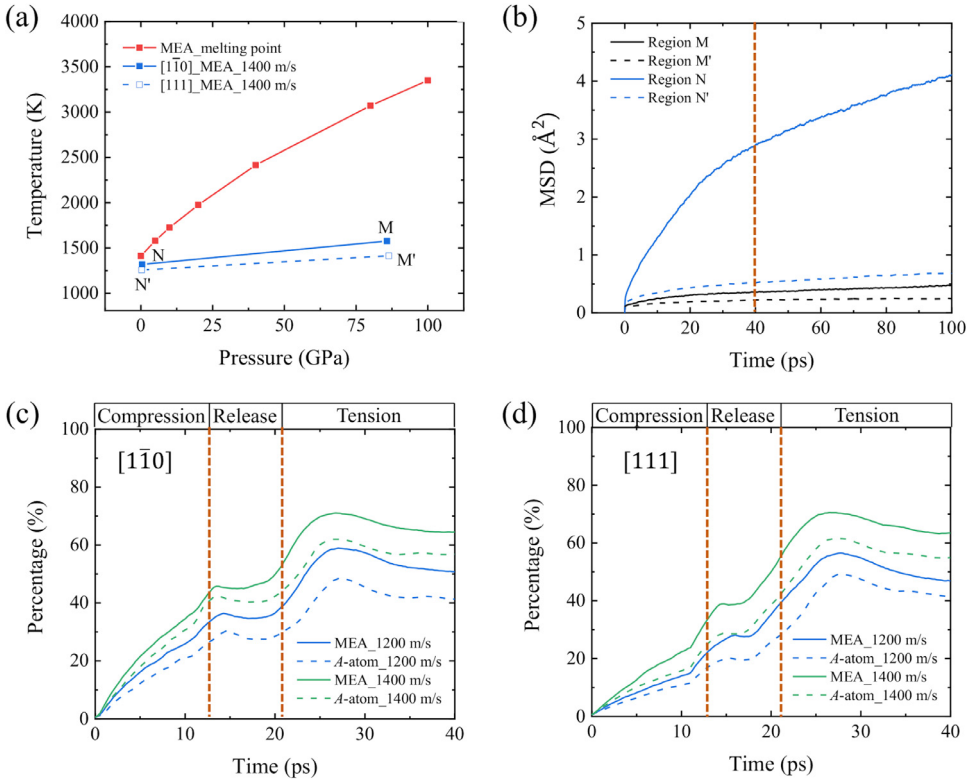

Fig. 3. (a) Melting point of CoCrNi MEA as a function of pressure. The temperatures of regions M, M′, N, and N′ at the shock compression and release stages for U_p = 1400 m/s in Fig. 2(c) and (f) are also displayed in (a). (b) Time evolution of the MSDs obtained by the extra equilibrium of 100 ps in regions M, M′, N, and N′. The vertical dashed line in (b) divides the MSD-time curves into two stages: first, a decrease in slope during 0–40 ps, followed by a nearly constant slope after 40 ps. Time evolution of the percentage of amorphous atoms in the CoCrNi MEA and *A*-atom sample under shock loading of U_p = 1200 m/s and 1400 m/s in the (c) [1$\bar{1}$0] and (d) [111] orientations, respectively. The vertical dashed lines in (c) and (d) divide the entire shock process into the compression, release, and tension stages.

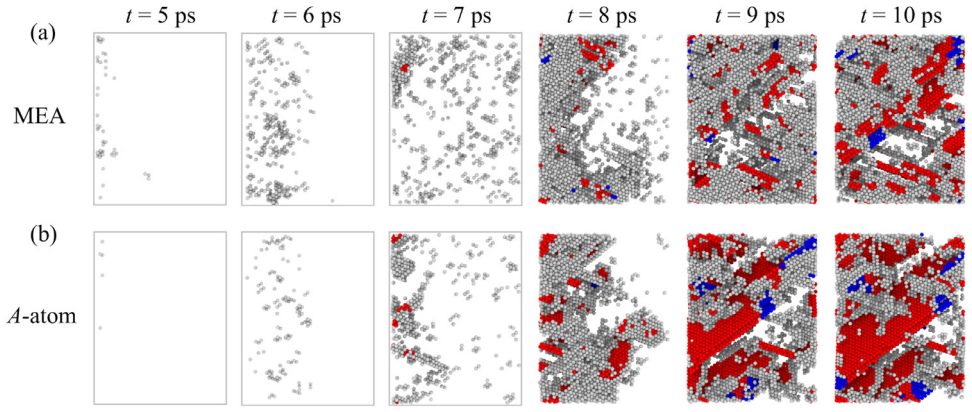

Fig. 4. Evolution of dislocations, SFs, twinning and amorphization in the local regions of (a) CoCrNi MEA and (b) *A*-atom pure metal under shock loading of U_p = 1400 m/s along [111] orientation. The visualization scheme is the same as that in Fig. 1.

Fig. 3 (c–d) compares the time evolution of the percentage of amorphous atoms in CoCrNi MEA and *A*-atom. For both U_p = 1200 m/s and 1400 m/s, amorphization begins in the compression stage and increases to over 40% of the sample in the tension stage. The CoCrNi MEA possesses more amorphous atoms than the *A*-atom material at U_p = 1200 m/s and 1400 m/s. LD in the CoCrNi MEA lowers the energy barrier for amorphization [45].

To probe the role of LD, we also compare the development of the shock-induced amorphization in the local regions of the CoCrNi MEA and *A*-atom metal when U_p = 1400 m/s in the [111] orientation, in which amorphization was the most pronouncedFig. 4. When the shock front arrives at the targeted region at 5 ps, only a few amorphous atoms are observed due to the initial perturbation of shock wave. As the shock compression proceeds, the amount of amorphous atoms increases rapidly at $t = 6$ ps and some of them aggregate into the clusters at $t = 7$ ps. Compared to the pure *A*-atom metal, the MEA possesses more amorphous clusters and their distribution is more uniform. This is related to the LD in MEA, which lowers the activation energy of amorphization in many regions throughout the sample. Later at 8 ps in the MEA, the amorphous clusters coalesce into a large amorphous region. Afterwards, at $t = 9$ and 10 ps, dislocations and twins form in the crystalline regions adjacent to these amorphous regions. Due to the larger amorphous content in the MEA than *A*-atom, these defect densities are much lower in the MEA. The consequences of LD are to

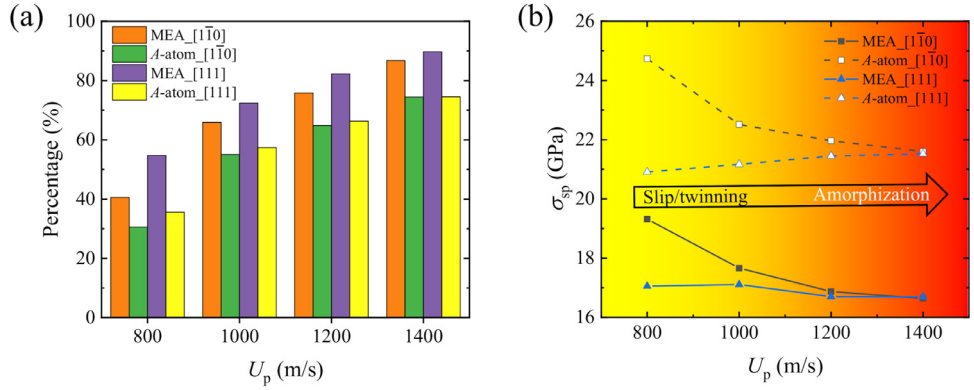

Fig. 5. (a) The percentage of amorphous atoms at the onset of spallation in the spallation region with the width of 15 nm along the *x* direction and (b) spall strength σ_{sp} for the [1$\bar{1}$0] and [111]-loading as a function of shock velocities U_p in CoCrNi MEA and *A*-atom pure metal.

promote amorphization and reduce the amount of crystal, in which the production of dislocations and twins is possible.

An extensive amount of amorphization is expected to change not only the spall strength but also the anisotropy in spall strength, due to its attenuating effect on the amount of dislocations and twins that can flow. In addition, the interactions between dislocations and twins also trigger the void formation and their amorphous interaction sites are also the nucleation sites of voids [36]. Thus, voids always form in the amorphous regions, which can form by the direct shock compression or the interactions between dislocations and twins. To quantify the extent, we compare the percentage of amorphous atoms at the onset of spallation within a 15 nm width of the spallation region. Fig. 5(a) indicates that the fraction of amorphous atoms is higher in the MEA than *A*-atom and is more significant in the [111] loading than [1$\bar{1}$0] loading. Concomitantly, as shown in Fig. 5(b), σ_{sp}, for both the MEA and *A*-atom, is higher for the [1$\bar{1}$0]-loading than the [111]-loading at the same U_p. Since voids nucleate and grow in the amorphous region during spallation [46], amorphization lowers the spall strength. Accordingly, the spall strength σ_{sp} of the *A*-atom pure metal surpasses its MEA counterpart. Below 1400 m/s, σ_{sp} is anisotropic for both MEA and *A*-atom pure metal. When U_p is raised to 1400 m/s, the anisotropy in σ_{sp} is nearly eliminated, since amorphization destroys the crystallographic anisotropy in the shock compression stage and the percentage of amorphous atoms in the spallation region exceeds 70% when spallation occurs.

In summary, large-scale MD simulations are conducted to investigate the shock-induced amorphization in CoCrNi MEA. Dislocation motion and twinning are the dominant deformation modes at low shock velocities and the material response is highly anisotropic, with larger densities of dislocations and twins at the compression stage and higher spall strength at the tension stage for shock loading in [1$\bar{1}$0] than in [111]. As the shock velocity increases, dislocation- and twinning-mediated deformation gives way to amorphization, where by the end of the compression stage, over 30% of the material is amorphous. Analysis of the melting temperature and diffusion coefficient shows that the amorphization is solid state and triggered by a sufficiently high shock velocity. Comparison with the shock response of the mean field version of the MEA without lattice distortion (LD), indicates that while LD is not the origin of amorphization, LD facilitates it, resulting in higher percentage of amorphous regions than without. With comparatively more amorphization, more voids form and the spall strength of the MEA becomes lower than that of the mean-field material without LD.

W.J. and I.J.B. would like to acknowledge support from the Office of Naval Research under Grant No. N000141712810. Use was made of computational facilities purchased with funds from the National Science Foundation (CNS-1725797) and administered by the Center for Scientific Computing (CSC). The CSC is supported by the California NanoSystems Institute and the Materials Research Science and Engineering Center (MRSEC; NSF DMR 1720256) at UC Santa Barbara. X.Y. would like to express his sincere gratitude for the financial support by National Science Foundation for Distinguished Young Scholars of China (11925203).

Declaration of Competing Interest

The authors declare that they have no known competing financial interests or personal relationships that could have appeared to influence the work reported in this paper.

Supplementary material

Supplementary material associated with this article can be found, in the online version, at 10.1016/j.scriptamat.2021.114379

References

[1] Y. Ye, Q. Wang, J. Lu, C. Liu, Y. Yang, Mater. Today 19 (2016) 349–362.
[2] E. Pickering, N. Jones, Int. Mater. Rev. 61 (2016) 183–202.
[3] Y. Zhang, T.T. Zuo, Z. Tang, M.C. Gao, K.A. Dahmen, P.K. Liaw, Z.P. Lu, Prog. Mater. Sci. 61 (2014) 1–93.
[4] H. Diao, R. Feng, K.A. Dahmen, P. Liaw, Curr. Opin. Solid State Mater. Sci. 21 (2017) 252–266.
[5] P. Shi, W. Ren, T. Zheng, Z. Ren, X. Hou, J. Peng, P. Hu, Y. Gao, Y. Zhong, P.K. Liaw, Nat. Commun. 10 (2019) 1–8.
[6] C. Lee, G. Song, M.C. Gao, R. Feng, P. Chen, J. Brechtl, Y. Chen, K. An, W. Guo, J.D. Poplawsky, et al., Acta Mater. 160 (2018) 158–172.
[7] B. Gludovatz, A. Hohenwarter, D. Catoor, E.H. Chang, E.P. George, R.O. Ritchie, Science 345 (2014) 1153–1158.
[8] B. Gludovatz, A. Hohenwarter, K.V. Thurston, H. Bei, Z. Wu, E.P. George, R.O. Ritchie, Nat. Commun. 7 (2016) 1–8.
[9] S. Chen, W. Li, X. Xie, J. Brechtl, B. Chen, P. Li, G. Zhao, F. Yang, J. Qiao, P.K. Liaw, J. Alloys Compd. 752 (2018) 464–475.
[10] S. Ma, Z. Jiao, J. Qiao, H. Yang, Y. Zhang, Z. Wang, Mater. Sci. Eng. A 649 (2016) 35–38.
[11] T. Zhang, Z. Jiao, Z. Wang, J. Qiao, Scr. Mater. 136 (2017) 15–19.
[12] J.M. Park, J. Moon, J.W. Bae, M.J. Jang, J. Park, S. Lee, H.S. Kim, Mater. Sci. Eng. A 719 (2018) 155–163.
[13] D. Foley, S. Huang, E. Anber, L. Shanahan, Y. Shen, A. Lang, C. Barr, D. Spearot, L. Lamberson, M. Taheri, Acta Mater. 200 (2020) 1–11.
[14] S. Zhao, Z. Li, C. Zhu, W. Yang, Z. Zhang, D.E. Armstrong, P.S. Grant, R.O. Ritchie, M.A. Meyers, Sci. Adv. 7 (2021) eabb3108.
[15] Y. Ma, F. Yuan, M. Yang, P. Jiang, E. Ma, X. Wu, Acta Mater. 148 (2018) 407–418.
[16] Z. Jiang, J. He, H. Wang, H. Zhang, Z. Lu, L. Dai, Mater. Res. Lett. 4 (2016) 226–232.
[17] Y. Yang, S. Yang, H. Wang, J. Alloys Compd. 851 (2020) 156883.
[18] Y. Yang, S. Yang, H. Wang, Mater. Sci. Eng. A (2020) 140440.
[19] R. Jeanloz, T.J. Ahrens, J. Lally, G. Nord, J. Christie, A. Heuer, Science 197 (1977) 457–459.
[20] M. Chen, J.W. McCauley, K.J. Hemker, Science 299 (2003) 1563–1566.
[21] S. Zhao, B. Kad, B.A. Remington, J.C. LaSalvia, C.E. Wehrenberg, K.D. Behler, M.A. Meyers, Proc. Natl. Acad. Sci. 113 (2016) 12088–12093.

[22] A. Gratz, L. DeLoach, T. Clough, W. Nellis, Science 259 (1993) 663–666.
[23] W.-H. Wang, C. Dong, C. Shek, Mat. Sci. Eng. R 44 (2004) 45–89.
[24] L. Zhong, J. Wang, H. Sheng, Z. Zhang, S.X. Mao, Nature 512 (2014) 177–180.
[25] S. Han, L. Zhao, Q. Jiang, J. Lian, Sci. Rep. 2 (2012) 1–5.
[26] M. Bhat, V. Molinero, E. Soignard, V. Solomon, S. Sastry, J. Yarger, C. Angell, Nature 448 (2007) 787–790.
[27] S. Zhao, B. Kad, C.E. Wehrenberg, B.A. Remington, E.N. Hahn, K.L. More, M.A. Meyers, Proc. Natl. Acad. Sci. 114 (2017) 9791–9796.
[28] H. Wang, D. Chen, X. An, Y. Zhang, S. Sun, Y. Tian, Z. Zhang, A. Wang, J. Liu, M. Song, et al., Sci. Adv. 7 (2021) eabe3105.
[29] S.M. Sharma, S. Sikka, Prog. Mater. Sci. 40 (1996) 1–77.
[30] E. Ma, Scr. Mater. 49 (2003) 941–946.
[31] W. Jian, X. Yao, L. Wang, X. Tang, S. Luo, J. Appl. Phys. 118 (2015) 015901.
[32] F. Zhao, B. Li, W. Jian, L. Wang, S. Luo, J. Appl. Phys. 118 (2015) 035904.
[33] W. Jian, B. Li, L. Wang, X. Yao, S. Luo, J. Appl. Phys. 118 (2015) 165902.
[34] W. Jian, X. Long, M. Tang, Y. Cai, X. Yao, S. Luo, Carbon 132 (2018) 520–528.
[35] L. Zhao, H. Zong, X. Ding, T. Lookman, Acta Mater. 209 (2021) 116801.
[36] Z. Xie, W.-R. Jian, S. Xu, I.J. Beyerlein, Z. Xiaoqing, Z. Wang, X. Yao, Acta Mater. 221 (2021) 117380.
[37] S. Zhao, E. Hahn, B. Kad, B.A. Remington, C. Wehrenberg, E.M. Bringa, M.A. Meyers, Acta Mater. 103 (2016) 519–533.
[38] S. Plimpton, J. Comp. Phys. 117 (1995) 1–19.
[39] Q.-J. Li, H. Sheng, E. Ma, Nat. Commun. 10 (2019) 3563.
[40] W.-R. Jian, Z. Xie, S. Xu, Y. Su, X. Yao, I.J. Beyerlein, Acta Mater. 199 (2020) 352–369.
[41] A. Stukowski, JOM 66 (2014) 399–407.
[42] J.R. Morris, C. Wang, K. Ho, C. Chan, Phys. Rev. B 49 (1994) 3109.
[43] S.Z. Chavoshi, S. Xu, S. Goel, Proc. R. Soc. A 473 (2017) 20170084.
[44] A. He, S. Duan, J.-L. Shao, P. Wang, C. Qin, J. Appl. Phys. 112 (2012) 074116.
[45] W.-R. Jian, L. Wang, W. Bi, S. Xu, I.J. Beyerlein, Appl. Phys. Lett. 119 (2021) 121904.
[46] Y. Ashkenazy, R.S. Averback, Appl. Phys. Lett. 86 (2005) 051907.